Integrating Deterministic and Stochastic Uncertainty in Terrestrial Laser Scanner-based Deformation Monitoring

Reza Naeimaei and Steffen Schön
Institut für Erdmessung (IfE), Leibniz Universität Hannover, Hannover, Germany
naeimaei@ife.uni-hannover.de; schoen@ife.uni-hannover.de

Elisabeth Ötsch and Hans Neuner
Research Group Engineering Geodesy, Geodesy and Geoinformation, TU Vienna, Vienna, Austria
elisabeth.oetsch@geo.tuwien.ac.at; hans.neuner@geo.tuwien.ac.at

Abstract. Terrestrial laser scanning (TLS) is widely used for deformation monitoring, where decisions about structural safety depend on a reliable description of measurement uncertainty. Classical congruency tests typically treat this uncertainty in a purely stochastic manner. However, remaining systematic effects from instrumental, atmospheric, and modelling sources may still influence the estimated deformation field. This becomes critical when the expected deformation is close to the magnitude of these unmodeled effects, as apparent displacements could be caused either by actual structural change or by systematic influences. In such situations of uncertainty, forcing a purely binary test decision may be difficult to justify.

To address this, this contribution introduces an interval-extended uncertainty propagation framework for TLS-based deformation monitoring. The uncertainty budget is separated into two components: stochastic variability, represented by random variables, and remaining systematic effects, represented as unknown-but-bounded intervals. Using sensitivity analysis of the TLS correction and measurement models, these bounded effects are propagated from physical influence parameters to the control-point (CP) domain of a B-spline surface model, and subsequently to the derived surface points (SP). This establishes a transparent link between physically interpretable TLS influence parameters and their impact on the final deformation decision.

The resulting congruency test extends the classical binary approach with a ternary decision structure: strict acceptance, ambiguity, and strict rejection. In the CP domain, the method utilizes a correlation-aware localization procedure based on the Schur complement. Conversely, in the SP domain, the propagated results are interpreted strictly as a pointwise diagnostic map. This distinction is essential because dense surface points are derived evaluations of the underlying CP deformation field; treating them as independent estimated parameters would be mathematically singular.

The results demonstrate that bounded systematic effects can significantly alter classical deformation decisions, and the interval-extended formulation makes this influence explicit. Rather than forcing uncertain cases into overconfident binary classifications, the proposed framework identifies regions where the deformation signal cannot be reliably separated from systematic uncertainty, providing a more cautious, transparent, and structurally safe basis for TLS-based deformation interpretation.

Keywords: Terrestrial Laser Scanning, Deformation Monitoring, Interval Analysis, Influence Parameters, Congruency Tests

1. Introduction

Terrestrial Laser Scanning (TLS) has fundamentally advanced geodetic deformation monitoring over recent decades, driven by significant progress in sensor technology and high-resolution data analysis methods (Niemeier, 2025). State-of-the-art applications now routinely achieve dense 3D displacement estimates for structural health monitoring, yet quantifying and reducing the complex uncertainty associated with these point clouds remains a critical challenge (Shi et al., 2025; Meyer et al., 2025). Classical deformation analysis relies heavily on rigorous statistical testing to identify structural movements over time (Caspary, 1987; Heunecke et al., 2013). However, millimetre-level deformation monitoring with TLS is often limited by systematic effects that remain even after applying sophisticated correction models.

Classical stochastic models describe random variability under standard distributional assumptions but do not provide rigorous bounds for these persistent systematic contributions. In uncertainty-modelling terms, this implies that random variability is accompanied by systematic effects: part of the uncertainty can be described stochastically, whereas another part is only available as bounded or admissible ranges (Beer et al., 2013). Building on recent advancements that integrate bounded systematic errors into TLS observation models (Naeimaei and Schön, 2025), this contribution extends these concepts to continuous surface monitoring. Here, remaining systematic effects are represented as bounded deviations and propagated as intervals through the estimation of B-spline surfaces.

The primary goal is to detect deformation reliably by comparing control-point (CP) coordinates between two measurement epochs while explicitly accounting for the correlation structure induced by the B-spline model. Specifically, this study aims to answer how bounded remaining systematic effects alter congruency decisions, and whether a ternary decision model is preferable to a forced binary one in uncertainty-dominated cases. The proposed workflow does not replace the classical stochastic test but complements it with a robust decision layer for scenarios in which the remaining systematics cannot be justified by a precise probability model.

The remainder of the paper is structured as follows. Section 2 introduces the mathematical framework for joint uncertainty modelling, including B-spline surface parameterisation and interval propagation. Section 3 describes the synthetic surface dataset, epoch configurations, and the Monte Carlo simulation design. Section 4 presents the classical congruency test and evaluates its empirical performance and limitations. Section 5 introduces the interval-extended framework and compares its diagnostic performance against the classical baseline. Finally, Section 7 draws conclusions and outlines directions for future research.

2. Mathematical Framework for Joint Uncertainty Modelling

To rigorously evaluate deformations at the millimetre level, it is essential to trace the impact of both random noise and residual systematic effects from the raw observations to the final deformation decision. This section formalizes the functional and stochastic models of the TLS measurements and introduces the framework for propagating bounded deterministic uncertainties.

2.1. B-spline surface parameterization and adjustment

The object surface is represented by a tensor-product B-spline surface (Piegl and Tiller, 1997):

$$\boldsymbol{S}(u,v) = \sum_{i=0}^{n} \sum_{j=0}^{m} N_{i,p}(u)\, N_{j,q}(v)\, \boldsymbol{P}_{i,j}, \tag{1}$$

with control points $\boldsymbol{P}_{i,j} \in \mathbb{R}^3$ and basis functions $N_{i,p}$ and $N_{j,q}$ of degrees p and q, respectively. In TLS-based surface modelling, tensor-product B-splines are attractive because they combine smoothness, local support, and a compact control-point representation that can be used directly for deformation analysis and stochastic modelling (Harmening, 2020; Kermarrec et al., 2020).

Using Cartesian coordinates observations $\boldsymbol{l}$, the approximation is formulated in a linearized Gauss–Markov model (Ötsch et al., 2025):

$$\boldsymbol{l} = \boldsymbol{A}\boldsymbol{x} + \boldsymbol{e}, \qquad \mathbb{E}[\boldsymbol{e}] = \boldsymbol{0}, \quad \mathrm{Cov}(\boldsymbol{e}) = \boldsymbol{\Sigma}_{ll}, \tag{2}$$

where $\boldsymbol{x}$ stacks all control-point coordinates and $\boldsymbol{A}$ is the design matrix. The stochastic model $\boldsymbol{\Sigma}_{ll}$ summarizes the precision and correlation assumptions of the TLS observations. Weighted least squares uses $\boldsymbol{P} = \boldsymbol{\Sigma}_{ll}^{-1}$ and the normal matrix $\boldsymbol{N} = \boldsymbol{A}^{\mathsf{T}}\boldsymbol{P}\boldsymbol{A}$.

Since the B-spline model is linear in the control-point coefficients, the functional model can be written as

$$\hat{\boldsymbol{x}} = \boldsymbol{x}_0 + \boldsymbol{K}\,(\boldsymbol{l} - \boldsymbol{A}\boldsymbol{x}_0), \tag{3}$$

where $\boldsymbol{x}_0$ denotes a linearization point and the observation-to-parameter mapping $\boldsymbol{K}$ is defined as:

$$\boldsymbol{K} \;=\; (\boldsymbol{A}^{\mathsf{T}}\boldsymbol{P}\boldsymbol{A})^{-1}\boldsymbol{A}^{\mathsf{T}}\boldsymbol{P} \;=\; \boldsymbol{N}^{-1}\boldsymbol{A}^{\mathsf{T}}\boldsymbol{P}. \tag{4}$$

Introducing the reduced observation vector $\tilde{\boldsymbol{l}} := \boldsymbol{l} - \boldsymbol{A}\boldsymbol{x}_0$, the estimated increment relative to the linearization point is $\delta\hat{\boldsymbol{x}} = \boldsymbol{K}\,\tilde{\boldsymbol{l}}$. The adjustment provides the covariance matrix $\boldsymbol{\Sigma}_{\hat{x}}$ through:

$$\boldsymbol{\Sigma}_{\hat{x}} = \hat{\sigma}_0^2\,\boldsymbol{Q}_{\hat{x}\hat{x}}, \qquad \boldsymbol{Q}_{\hat{x}\hat{x}} = (\boldsymbol{A}^{\top}\boldsymbol{P}\boldsymbol{A})^{-1}. \tag{5}$$

2.2. TLS measurement and bounded correction model

Cartesian coordinates are computed from TLS polar measurements (range r, horizontal angle φ, vertical angle θ) and correction functions $(C_r, C_\varphi, C_\theta)$:

$$\boldsymbol{p} = \begin{bmatrix} x \\ y \\ z \end{bmatrix} = \begin{bmatrix} (r + C_r)\sin(\theta + C_\theta)\sin(\varphi + C_\varphi) \\ (r + C_r)\sin(\theta + C_\theta)\cos(\varphi + C_\varphi) \\ (r + C_r)\cos(\theta + C_\theta) \end{bmatrix}. \tag{6}$$

Following the correction model in Medić et al. (2019), the polar corrections are parameterized as

$$C_r(r,\theta;\boldsymbol{s}) \;=\; x_2\sin\theta + x_{10}, \tag{7}$$

$$C_\varphi(r,\theta;\boldsymbol{s}) \;=\; \frac{x_{1z}}{r\tan\theta} + \frac{x_3}{r\sin\theta} + \frac{x_{5z} - x_7}{\tan\theta} + \frac{2x_6}{\sin\theta} + \frac{x_{1n}}{r}, \tag{8}$$

$$C_\theta(r,\theta;\boldsymbol{s}) \;=\; \frac{x_{1n}\cos\theta}{r} + \frac{x_2\cos\theta}{r} + x_4 + x_{5n}\cos\theta - \frac{x_{1z}\sin\theta}{r} - x_{5z}\sin\theta, \tag{9}$$

where $\boldsymbol{s} = \{x_{1n}, x_{1z}, x_2, x_3, x_{10}, x_4, x_{5n}, x_{5z}, x_6, x_7\}^{\mathsf{T}}$ collects the influential calibration parameters. Each influential parameter is treated as an unknown-but-bounded deviation,

$$s_k \in \left[s_k^* - \Delta s_k, \quad s_k^* + \Delta s_k\right].$$

This formulation is consistent with the interval-based treatment of systematic effects proposed by Naeimaei and Schön (2025), where remaining calibration uncertainties are modeled as admissible bounded deviations. In this paper, the interval radius Δs_k is derived from the simulated calibration sets in Table I as half of the observed range,

$$\Delta s_k \;=\; 0.5 \cdot \left|\max s_k - \min s_k\right|, \tag{10}$$

Table I. Instrument error-source parameters used in the synthetic dataset. Sets 1 through 4 represent different calibration states across simulated epochs. The interval radius Δs_k is derived as half the maximum range across all four sets.

Parameter	Description	Set 1	Set 2	Set 3	Set 4	Radius Δs_k
x_{1n} [mm]	Horizontal beam offset	0.07	0.08	0.05	0.05	0.015
x_{1z} [mm]	Vertical beam offset	0.08	0.31	0.21	0.14	0.115
x_2 [mm]	Horizontal axis offset	−0.12	−0.11	−0.12	−0.14	0.015
x_3 [mm]	Mirror offset	−0.02	0.00	−0.06	−0.03	0.030
x_{10} [mm]	Rangefinder offset	−0.16	0.03	0.01	−0.03	0.095
x_4 [arcsec]	Vertical index offset	4.20	5.10	5.17	4.51	0.485
x_{5n} [arcsec]	Horizontal beam tilt	4.50	4.67	5.62	5.38	0.560
x_{5z} [arcsec]	Vertical beam tilt	−12.00	−14.71	−14.33	−16.78	2.390
x_6 [arcsec]	Mirror tilt	4.19	3.59	4.11	3.41	0.390
x_7 [arcsec]	Horizontal axis error	−22.35	−25.38	−26.31	−33.50	5.575

which yields symmetric intervals around nominal values s_k^*. The parameterization and magnitude levels in Table I are based on the calibration model proposed by Medić et al. (2019).

2.3. Sensitivity analysis and interval propagation

To evaluate the impact of these bounded systematic errors on the estimated control points, we apply an interval-extended least-squares adjustment (IELSA). Sensitivity analysis quantifies how small changes in model inputs affect the model output (Kutterer, 1999; Naeimaei and Schön, 2025).

Let a model output $f(\boldsymbol{s})$ depend on influence parameters $\boldsymbol{s}$. The first-order differential is $\mathrm{d}f = \boldsymbol{F}\,\mathrm{d}\boldsymbol{s}$, with Jacobian row vector $\boldsymbol{F}$. If the influence parameters are bounded by intervals $\boldsymbol{\Delta}_s$, the corresponding first-order interval radius is:

$$\Delta f = \sum_{i=1}^{n} \left| \frac{\partial f(\boldsymbol{s}^*)}{\partial s_i} \right| \Delta s_i \;=\; |\boldsymbol{F}|\,\boldsymbol{\Delta}_s. \tag{11}$$

Applying Eq. (11) to the TLS correction model—where the notation $|\cdot|$ applied to a matrix denotes the element-wise absolute value—yields observation-level interval radii $\boldsymbol{\Delta}_l = |\boldsymbol{F}|\,\boldsymbol{\Delta}_s$. Propagating these bounds through the linearized least-squares estimator (using the mapping matrix $\boldsymbol{K}$ from Eq. 4) yields the parameter-level enclosure for the control points:

$$\boldsymbol{\Delta}_{\hat{x}} = |\boldsymbol{K}\boldsymbol{F}|\,\boldsymbol{\Delta}_s. \tag{12}$$

This formulation is typically tighter than the two-step bound $|\boldsymbol{K}|\,|\boldsymbol{F}|\,\boldsymbol{\Delta}_s$ because possible cancellations are preserved before taking absolute values.

3. Experimental Dataset and Preprocessing

3.1. Monte Carlo simulation of noise and bounded systematics

To rigorously evaluate the congruency testing framework, a controlled Monte Carlo simulation environment is established. The evaluation relies on generating 1000 Monte Carlo realizations per configuration to adequately capture stochastic variability. Given a predefined scan station coordinate, true Cartesian coordinates of the SP are first transformed into polar pseudo-observations (r, φ, θ). For each realization, these observations are then corrupted by two distinct uncertainty components:

1. **Stochastic Noise:** Zero-mean Gaussian noise is added independently to each polar component with standard deviations

$$\sigma_r = 1\,\mathrm{mm}, \qquad \sigma_\varphi = \sigma_\theta = 4.44\,\mathrm{mgon}\ (= 0.004^\circ). \tag{13}$$

2. **Deterministic Bias:** Using the correction model established in Eq. (6), specific calibration parameter sets (Table I) are injected. Set 1 is applied to the reference state, and Set 4 to the subsequent comparison states. This intentional mismatch simulates realistic, unmodeled calibration inconsistencies between measurement campaigns.

This general simulation pipeline provides a foundation for generating specific structural deformation scenarios with known ground truth.

3.2. Synthetic surface and deformation scenarios

Applying the Monte Carlo framework described above, an experimental dataset is constructed consisting of a reference epoch $\mathcal{E}_{\mathrm{ref}}$ and a comparison epoch $\mathcal{E}_{\mathrm{comp}}$. The monitored object is modeled as a tensor-product B-spline surface with a fixed parameterization across epochs, enabling direct epoch differencing in the CP domain without remeshing.

To simulate localized deformations, specific CPs in $\mathcal{E}_{\mathrm{comp}}$ are displaced by 10 mm and 20 mm along the y-direction (Figure 1). Because B-spline surfaces possess local support, these discrete CP movements do not translate the entire surface; instead, they induce a continuous, smoothly tapering deformation. The surface displacement peaks within the region of maximum basis-function influence but remains strictly bounded by the CP displacement magnitudes. Consequently, while CP ground truth is defined by the discrete displacement vector, surface ground truth is determined by a *region-of-influence* mask, effectively partitioning the surface into stable and deformed regions based on whether a point's local support includes a displaced CP.

The 10 mm and 20 mm magnitudes represent realistic macro-deformations and were deliberately chosen to lie safely above the TLS stochastic noise floor ($\sigma \approx 2\,\mathrm{mm}$) and the theoretical Minimum Detectable Deformation (MDD). Enforcing this high signal-to-noise ratio ensures that any false alarms or missed detections observed during testing are strictly driven by unmodeled systematic biases, spatial correlations, or B-spline topology, rather than simple stochastic noise limits.

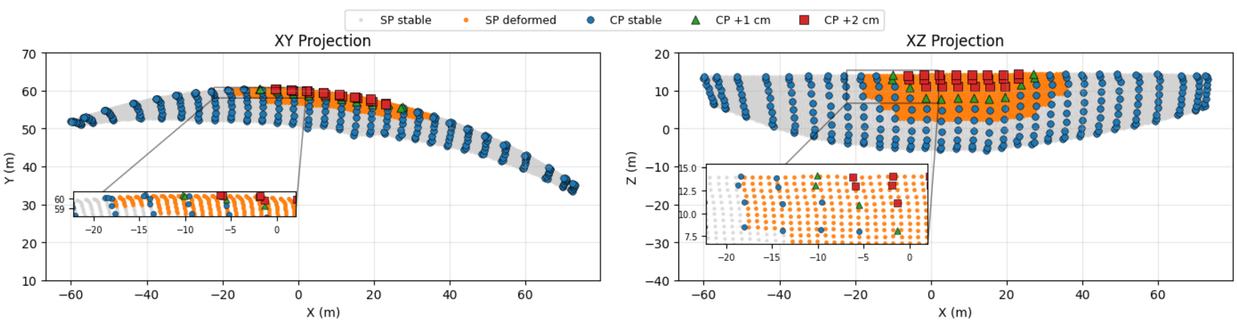

Figure 1. Visualization of the synthetic deformation scenario. (a) Nominal B-spline surface and control-point network ($\mathcal{E}_{\mathrm{ref}}$). (b) Deformed surface ($\mathcal{E}_{\mathrm{comp}}$). (c) Injected 1 cm and 2 cm displacements in the discrete CP domain. (d) Resulting continuous deformation in the SP domain, illustrating the spatial influence of the B-spline local support.

4. Classical congruency test

This section presents classical two-epoch congruency tests in the control-point (CP) domain and on the reconstructed surface. All tests are formulated with the full variance–covariance matrix of the estimated control points within each epoch; hence both intra-point XYZ correlations and inter-point correlations are retained.

4.1. Global test in the Control points domain

Let $\hat{\boldsymbol{x}}_1, \hat{\boldsymbol{x}}_2 \in \mathbb{R}^{3n_{\mathrm{cp}}}$ be the stacked CP coordinate vectors estimated in Epoch 1 and Epoch 2, ordered as $[x_1, y_1, z_1, \ldots, x_{n_{\mathrm{cp}}}, y_{n_{\mathrm{cp}}}, z_{n_{\mathrm{cp}}}]^\top$. The epoch difference is

$$\hat{\boldsymbol{d}} = \hat{\boldsymbol{x}}_2 - \hat{\boldsymbol{x}}_1. \tag{14}$$

Neglecting cross-covariances between the two epoch solutions, the covariance of $\hat{\boldsymbol{d}}$ is

$$\boldsymbol{\Sigma}_{\hat{d}\hat{d}} = \boldsymbol{\Sigma}_{\hat{x}_1} + \boldsymbol{\Sigma}_{\hat{x}_2}, \tag{15}$$

where $\boldsymbol{\Sigma}_{\hat{x}_k} = \hat{\sigma}^2_{0,k}\, \boldsymbol{Q}_{\hat{x}_k\hat{x}_k}$ for Epoch $k \in \{1, 2\}$.

4.1.1. *Measurement model for the epoch differences*

In the classical test, the estimated difference vector is modelled as

$$\hat{\boldsymbol{d}} = \boldsymbol{\mu} + \boldsymbol{e}, \qquad \mathbb{E}[\boldsymbol{e}] = \boldsymbol{0}, \qquad \mathrm{Cov}(\boldsymbol{e}) = \boldsymbol{\Sigma}_{dd}, \tag{16}$$

where $\boldsymbol{\mu}$ denotes the unknown true displacement vector and $\boldsymbol{e}$ collects stochastic estimation errors. The hypotheses are

$$H_0 : \ \boldsymbol{\mu} = \boldsymbol{0}, \qquad H_1 : \ \boldsymbol{\mu} \neq \boldsymbol{0}. \tag{17}$$

4.1.2. *Compatibility of variance factors and pooled scale*

Before combining epochs, the compatibility of the a posteriori variance factors $\hat{\sigma}^2_{0,1}$ and $\hat{\sigma}^2_{0,2}$ is verified via an F-test (Caspary, 1987; Heunecke et al., 2013). Across all simulated realizations, they remain statistically compatible. Because both epochs share identical measurement configurations and parameterizations ($f_1 = f_2$), the pooled variance simplifies to their arithmetic mean:

$$\hat{\sigma}^2_0 = \frac{\hat{\sigma}^2_{0,1} + \hat{\sigma}^2_{0,2}}{2}, \tag{18}$$

where the total redundancy is defined as $f := f_1 + f_2$.

4.1.3. *Global test statistic*

Using the cofactor matrix $\boldsymbol{Q}_{\hat{d}\hat{d}} = \boldsymbol{Q}_{\hat{x}_1\hat{x}_1} + \boldsymbol{Q}_{\hat{x}_2\hat{x}_2}$ and $\boldsymbol{\Sigma}_{\hat{d}\hat{d}} = \hat{\sigma}^2_0 \boldsymbol{Q}_{\hat{d}\hat{d}}$, the global congruency quadratic form is based on:

$$R_{\mathrm{glob}} = \hat{\boldsymbol{d}}^\top \boldsymbol{Q}^{-1}_{\hat{\boldsymbol{d}}\hat{\boldsymbol{d}}}\, \hat{\boldsymbol{d}}, \tag{19}$$

With $h = \mathrm{rank}(\boldsymbol{Q}_{\hat{d}\hat{d}})$, the normalized statistic is

$$T_{\mathrm{glob}} = \frac{(R_{\mathrm{glob}}/h)}{\hat{\sigma}^2_0}. \tag{20}$$

Under H_0,

$$T_{\mathrm{glob}} \sim F(h, f), \qquad k_\alpha := F_{h,f;\,1-\alpha}, \qquad T_{\mathrm{glob}} \geq k_\alpha \ \Rightarrow \ \text{reject } H_0. \tag{21}$$

4.2. Local test in the control point domain

Following a global rejection, local diagnosis aims to identify specific control points contributing to the deformation signal. Due to the inherent stochastic correlations among the estimated points, we apply the successive decomposition of the global quadratic form, a standard multiple-testing procedure established by Caspary (1987) and further detailed by Heunecke et al. (2013). The vector $\hat{\boldsymbol{d}}$ and cofactor matrix $\boldsymbol{Q}_{\hat{d}\hat{d}}$ are partitioned into the target point p and the remaining points n:

$$\hat{\boldsymbol{d}} = \begin{pmatrix} \hat{\boldsymbol{d}}_n \\ \hat{\boldsymbol{d}}_p \end{pmatrix}, \qquad \boldsymbol{Q}_{\hat{d}\hat{d}} = \begin{pmatrix} \boldsymbol{Q}_{nn} & \boldsymbol{Q}_{np} \\ \boldsymbol{Q}_{pn} & \boldsymbol{Q}_{pp} \end{pmatrix}. \tag{22}$$

To account for cross-covariances, the conditional displacement $\bar{\boldsymbol{d}}_p$ and its associated cofactor matrix (Schur complement) $\boldsymbol{Q}_{p|n}$ are computed as:

$$\bar{\boldsymbol{d}}_p = \hat{\boldsymbol{d}}_p - \boldsymbol{Q}_{pn}\,\boldsymbol{Q}_{nn}^{-1}\,\hat{\boldsymbol{d}}_n, \qquad \boldsymbol{Q}_{p|n} = \boldsymbol{Q}_{pp} - \boldsymbol{Q}_{pn}\,\boldsymbol{Q}_{nn}^{-1}\,\boldsymbol{Q}_{np}. \tag{23}$$

The local quadratic contribution is $R_p = \bar{\boldsymbol{d}}_p^\top\,\boldsymbol{Q}_{p|n}^{-1}\,\bar{\boldsymbol{d}}_p$. For a 3D point, the normalized statistic $T_p = (R_p/3)/\hat{\sigma}_0^2$ is compared against the threshold $F_{3,f;\,1-\alpha}$.

Localization is an iterative elimination process: the point maximizing T_p is removed, and the system is recomputed until the remaining set passes a global congruency test, ensuring a statistically consistent reference frame. Throughout this decomposition, the initial pooled variance factor $\hat{\sigma}_0^2$ is strictly retained to prevent masking effects and maintain consistent test power.

4.3. Pointwise diagnostic map in the surface domain

After a global rejection in the CP domain, the deformation field is evaluated on the reconstructed surface. Since the surface is a deterministic linear mapping of the estimated control points, the SP displacements do not represent an independent set of estimated parameters. Therefore, the SP analysis is not used as a second rigorous localization procedure equivalent to the CP-domain Schur-complement localization. Instead, it is used as a pointwise diagnostic evaluation to visualize how the CP-domain deformation field is expressed over the continuous surface.

The displacement of a surface point at parameter location (u, v) is calculated as:

$$\hat{\boldsymbol{d}}_S(u, v) = \boldsymbol{B}(u, v)\hat{\boldsymbol{d}}. \tag{24}$$

Here, $\boldsymbol{B}(u, v) \in \mathbb{R}^{3\times 3n_{\text{cp}}}$ collects the tensor-product basis functions $N_{i,p}(u)N_{j,q}(v)$ associated with the local support. By linear propagation of the full CP-domain covariance, the associated surface cofactor matrix is:

$$\boldsymbol{Q}_{\hat{d}_S\hat{d}_S}(u, v) = \boldsymbol{B}(u, v)\,\boldsymbol{Q}_{\hat{d}\hat{d}}\,\boldsymbol{B}(u, v)^\top. \tag{25}$$

The normalized surface statistic is formulated analogously to the local CP test:

$$T_{\text{surf}}(u, v) = \frac{(\hat{\boldsymbol{d}}_S^\top\,\boldsymbol{Q}_{\hat{d}_S\hat{d}_S}^{-1}\,\hat{\boldsymbol{d}}_S/3)}{\hat{\sigma}_0^2}, \tag{26}$$

where $T_{\text{surf}}(u, v) \sim F(3, f)$ under H_0. A surface location is flagged as deformed if $T_{\text{surf}}(u, v) \geq F_{3,f;\,1-\alpha}$.

Unlike the CP domain, rigorous successive elimination (Eq. 23) is omitted in the SP domain. Because dense surface points are strictly derived evaluations rather than independent estimated parameters, their covariance matrix is highly rank-deficient. This makes local Schur-complement steps mathematically singular. Consequently, the pointwise surface statistic (T_{surf}) serves strictly as a diagnostic map. This necessary simplification inherently neglects spatial cross-covariances between adjacent surface points.

4.4. Empirical performance and limitations of the classical test

The classical congruency tests are executed at $\alpha = 0.05$. Because the CP domain utilizes rigorous successive elimination while the SP domain relies on a pointwise diagnostic map, their performances must be evaluated separately.

Table II. Averaged classical confusion matrix evaluated in the CP domain across 1000 Monte Carlo realizations (rigorous successive elimination).

Ground Truth	Total	Pred. Stable	Pred. Deformed
Stable	266	TN: 250.4 (94.1%)	FP: 15.6 (5.9%)
Deformed	34	FN: 0.2 (0.6%)	TP: 33.8 (99.4%)

Table II summarizes the CP domain performance. The false-alarm rate (5.9%) slightly exceeds the nominal level, indicating that remaining systematic biases influence the test statistics despite rigorous correlation handling.

Table III. Averaged classical confusion matrix evaluated in the SP domain across 1000 Monte Carlo realizations (pointwise diagnostic map).

Ground Truth	Total	Pred. Stable	Pred. Deformed
Stable	3609	TN: 3097.5 (85.8%)	FP: 511.5 (14.2%)
Deformed	891	FN: 292.9 (32.9%)	TP: 598.1 (67.1%)

In the dense SP domain (Table III), 14.2% of physically stable surface points are flagged as deformed by the pointwise diagnostic evaluation. This value should not be interpreted in the same way as the CP-domain false-alarm rate, because the SP map consists of many spatially dependent derived evaluations and no multiple-testing correction is applied. The result nevertheless illustrates an important practical issue: when the continuous surface is evaluated pointwise, remaining systematic effects and strong spatial dependence can produce extended regions of apparent deformation. The SP map is therefore useful as a diagnostic visualization, but not as a fully correlation-aware statistical localization procedure.

To interpret the high CP detection rates, we perform a detectability analysis. Under H_1, the local 3D CP statistic follows a non-central F-distribution with non-centrality parameter:

$$\lambda = \frac{\boldsymbol{\mu}_{\text{true}}^{\mathsf{T}} \, \boldsymbol{Q}_{p|n}^{-1} \, \boldsymbol{\mu}_{\text{true}}}{\hat{\sigma}_0^2}, \tag{27}$$

where $\boldsymbol{\mu}_{\text{true}}$ is the true displacement and $\boldsymbol{Q}_{p|n}$ is the Schur-complement cofactor (Eq. 23). Figure 2 shows that both displacement groups lie far above their 80% detectability thresholds (2.71 mm and 3.13 mm). Thus, the near-unit true-positive rate in the CP domain is theoretically expected and should not be overinterpreted as a general method strength.

Classically termed *minimum detectable bias* (Baarda, 1967), we refer to this as *minimum detectable deformation* (MDD) to avoid confusion with the bounded systematic biases (Section 5). For a unit direction $\boldsymbol{u}$, the directional MDD is:

$$\mathrm{MDD}(\boldsymbol{u}) = \sqrt{\lambda_{\mathrm{MDD}}\, \boldsymbol{u}^{\mathsf{T}}\, \hat{\sigma}_0^2\, \boldsymbol{Q}_{p|n}\, \boldsymbol{u}}, \tag{28}$$

where λ_{MDD} is derived from the target power $P(F(3, f, \lambda_{\mathrm{MDD}}) \geq F_{3,f;\,1-\alpha}) = 1 - \beta$. Therefore, Figure 2 depicts directional MDD_{80} values, not universal thresholds.

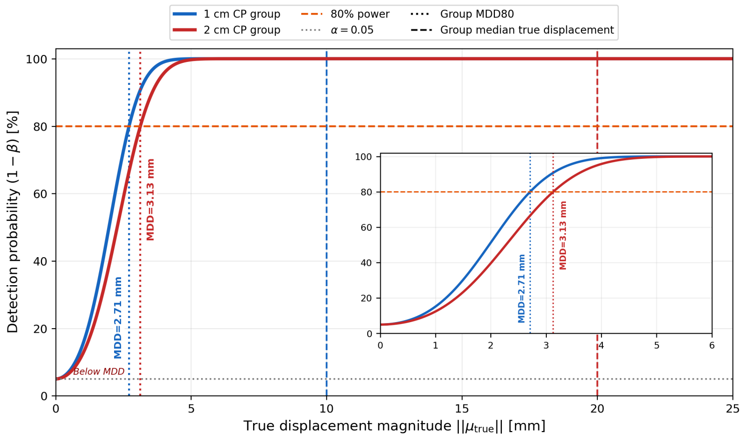

Figure 2. Analytical power curves of the local 3D CP congruency test. Both displacement groups (10 mm, 20 mm) lie far above the corresponding MDD thresholds.

Importantly, CP-based detectability does not guarantee uniform SP detectability. Surface displacements taper across the B-spline support, so edge deformations often fall below the MDD, increasing SP missed detections (Figure 3). Ultimately, the elevated SP false-alarm rate reveals a fundamental limit in purely stochastic monitoring: when rigorous correlation handling becomes mathematically inaccessible on dense surfaces, the resulting necessary simplifications force overconfident binary decisions. This specific limitation—the inability to safely absorb the uncertainty caused by methodological simplifications and unmodeled biases—directly motivates the interval-extended framework in Section 5.

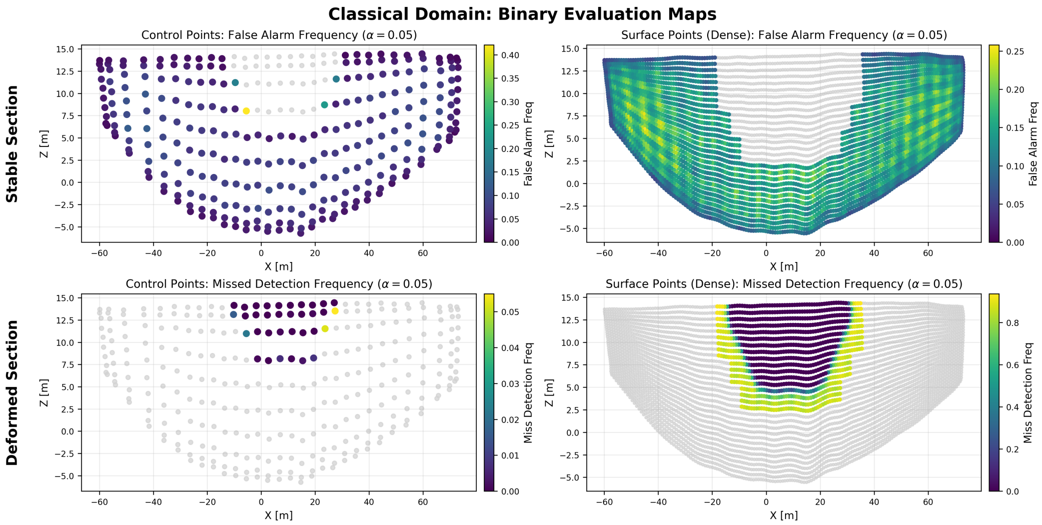

Figure 3. Spatial distribution of empirical error frequencies across 1000 Monte Carlo realizations ($\alpha = 0.05$). Left: missed-detection frequency on the deformed subset. Right: false-alarm frequency on the stable subset.

5. Interval-extended congruency test

This section extends the classical congruency test by explicitly accounting for remaining systematic effects in the epoch differences. In addition to stochastic estimation noise, the epoch-difference vector is affected by an unknown but bounded systematic contribution. The resulting decision is therefore ternary rather than binary.

5.1. Global test in the CP domain

5.1.1. *Measurement model for the epoch differences*

Let $\hat{\boldsymbol{d}}$ denote the CP epoch-difference vector introduced in Section 4, with covariance $\boldsymbol{\Sigma}_{dd} = \hat{\sigma}_0^2\, \boldsymbol{Q}_{dd}$. In the interval-extended model, the observation equation is written as

$$\hat{\boldsymbol{d}} = \boldsymbol{\mu} + \boldsymbol{b} + \boldsymbol{e}, \qquad \mathbb{E}[\boldsymbol{e}] = \boldsymbol{0}, \qquad \mathrm{Cov}(\boldsymbol{e}) = \boldsymbol{\Sigma}_{dd}, \qquad \boldsymbol{b} \in \mathcal{B}, \tag{29}$$

where $\boldsymbol{b}$ is an additional systematic contribution bounded by an admissible set $\mathcal{B}$ (Naeimaei and Schön, 2026). The hypotheses remain $H_0 : \boldsymbol{\mu} = \boldsymbol{0}, \qquad H_1 : \boldsymbol{\mu} \neq \boldsymbol{0}$.

5.1.2. *Bias set representation (error box)*

To obtain a simple and transparent uncertainty model, the systematic contribution is enclosed by an axis-aligned box in CP-difference space:

$$\mathcal{B}_\square = [-\Delta_{\boldsymbol{d}},\, +\Delta_{\boldsymbol{d}}] = \left\{ \boldsymbol{b} \in \mathbb{R}^{3n_{\mathrm{cp}}} :\; -\Delta_{\boldsymbol{d}} \le \boldsymbol{b} \le +\Delta_{\boldsymbol{d}} \right\}, \tag{30}$$

where $\Delta_{\boldsymbol{d}}$ denotes the componentwise radius of the admissible systematic bias.

5.1.3. *Partial cancellation of systematic effects*

While some systematic effects may partially cancel during epoch differencing, perfect cancellation is rare in practice because station setups, geometry, and calibration conditions easily vary between measurements. Therefore, the influence parameters are partitioned into two groups: parameters assumed to remain consistent across epochs (C) and parameters that may vary between epochs (E).

In this study, only the rangefinder offset x_{10} and the vertical index offset x_4 are assumed to vary between epochs, while all other parameters are assumed stable. The corresponding CP-domain bias radius is modeled as:

$$\Delta_{\boldsymbol{d}} = |(\boldsymbol{KF}_2 - \boldsymbol{KF}_1)|_{(:,C)}\; \Delta_{\boldsymbol{s}_C} + (|\boldsymbol{KF}_2| + |\boldsymbol{KF}_1|)_{(:,E)}\, \Delta_{\boldsymbol{s}_E}. \tag{31}$$

As a result, stable contributions are partially reduced by differencing, whereas epoch-dependent contributions are conservatively accumulated.

5.1.4. *Global ternary decision*

Using the same quadratic form as the classical global test, but corrected by an admissible bias vector, the interval-dependent statistic is

$$T_{\mathrm{glob}}(\boldsymbol{b}) = \frac{1}{h\hat{\sigma}_0^2} (\hat{\boldsymbol{d}} - \boldsymbol{b})^\top \boldsymbol{Q}_{dd}^{-1} (\hat{\boldsymbol{d}} - \boldsymbol{b}), \qquad \boldsymbol{b} \in \mathcal{B}_\square, \tag{32}$$

with $h = \mathrm{rank}(\boldsymbol{Q}_{dd})$. Since the exact bias realization is unknown, the decision is based on the extremal values

$$T_{\mathrm{glob,min}} = \min_{\boldsymbol{b} \in \mathcal{B}_\square} \left(T_{\mathrm{glob}}(\boldsymbol{b}) \right), \qquad T_{\mathrm{glob,max}} = \max_{\boldsymbol{b} \in \mathcal{B}_\square} \left(T_{\mathrm{glob}}(\boldsymbol{b}) \right). \tag{33}$$

Note that while calculating $T_{\mathrm{glob,min}}$ is a standard convex quadratic program solvable in polynomial time, computing the exact $T_{\mathrm{glob,max}}$ over a high-dimensional box is an NP-hard optimization problem. However, for the global diagnostic decision, evaluating $T_{\mathrm{glob,min}}$ is strictly sufficient to determine if the local diagnosis must be triggered. With the same critical value $k_\alpha = F_{h,f;1-\alpha}$ as in the classical test, the decision rule becomes

$$\text{strict accept } H_0 \quad \text{if } T_{\mathrm{glob,max}} < k_\alpha, \qquad \text{strict reject } H_0 \quad \text{if } T_{\mathrm{glob,min}} > k_\alpha, \quad \text{ambiguous} \quad \text{otherwise.} \tag{34}$$

Hence, congruency is accepted only if all admissible biases support H_0, and rejected only if all admissible biases contradict it.

5.2. Local test in the CP domain

If the global test rejects H_0 or remains ambiguous, local diagnosis is performed for individual CPs. As in the classical approach, the test is based on correlation-aware single-point diagnosis, but now under bounded systematic bias. Partition the epoch-difference vector, the admissible bias vector, and the cofactor matrix into the target point p and all remaining points n:

$$\hat{\boldsymbol{d}} = \begin{pmatrix} \hat{\boldsymbol{d}}_n \\ \hat{\boldsymbol{d}}_p \end{pmatrix}, \qquad \boldsymbol{b} = \begin{pmatrix} \boldsymbol{b}_n \\ \boldsymbol{b}_p \end{pmatrix}, \qquad \boldsymbol{Q}_{dd} = \begin{pmatrix} \boldsymbol{Q}_{nn} & \boldsymbol{Q}_{np} \\ \boldsymbol{Q}_{pn} & \boldsymbol{Q}_{pp} \end{pmatrix}, \tag{35}$$

with $\hat{\boldsymbol{d}}_p, \boldsymbol{b}_p \in \mathbb{R}^3$ and $\boldsymbol{Q}_{pp} \in \mathbb{R}^{3\times 3}$. Analogous to the classical case, the correlation-aware local displacement of point p, conditional on the remaining points, is:

$$\bar{\boldsymbol{d}}_p(\boldsymbol{b}) = (\hat{\boldsymbol{d}}_p - \boldsymbol{b}_p) - \boldsymbol{Q}_{pn}\boldsymbol{Q}_{nn}^{-1}(\hat{\boldsymbol{d}}_n - \boldsymbol{b}_n), \tag{36}$$

with the same Schur-complement cofactor matrix $\boldsymbol{Q}_{p|n}$ as in the classical case. This expression can be written in affine form as:

$$\bar{\boldsymbol{d}}_p(\boldsymbol{b}) = \bar{\boldsymbol{d}}_p - \boldsymbol{M}_p\boldsymbol{b}, \qquad \boldsymbol{M}_p = [-\boldsymbol{Q}_{pn}\boldsymbol{Q}_{nn}^{-1} \quad \boldsymbol{I}_3] \tag{37}$$

where $\bar{\boldsymbol{d}}_p$ is the conditional displacement and $\boldsymbol{M}_p$ is the corresponding bias mapping.

5.2.1. *Local bounding and ternary decision*

To avoid repeated optimization in the full CP space, the global bias set is projected into a local 3D uncertainty set for each control point. This set is conservatively approximated by an axis-aligned bounding box, enabling efficient evaluation of the local test statistic:

$$\boldsymbol{u}_p \in [-\Delta_{\bar{\boldsymbol{d}}_p}, +\Delta_{\bar{\boldsymbol{d}}_p}], \qquad \Delta_{\bar{\boldsymbol{d}}_p} = |\boldsymbol{M}_p|\Delta_{\boldsymbol{d}}. \tag{38}$$

For any admissible local bias $\boldsymbol{u}_p$, the test statistic is:

$$T_p(\boldsymbol{u}_p) = \frac{1}{3\hat{\sigma}_0^2}(\bar{\boldsymbol{d}}_p - \boldsymbol{u}_p)^\top \boldsymbol{Q}_{p|n}^{-1}(\bar{\boldsymbol{d}}_p - \boldsymbol{u}_p). \tag{39}$$

Since the exact bias realization is unknown, the extremal values within this bounding box are evaluated:

$$T_{p,\min} = \min_{\boldsymbol{u}_p}\left(T_p(\boldsymbol{u}_p)\right), \qquad T_{p,\max} = \max_{\boldsymbol{u}_p}\left(T_p(\boldsymbol{u}_p)\right). \tag{40}$$

The local ternary decision is obtained analogously to the global case using the critical value $k_\alpha = F_{3,f;1-\alpha}$:

$$\begin{array}{ll} \text{strict accept } H_0 \text{ for CP } p & \text{if } T_{p,\max} < k_\alpha, \\ \text{strict reject } H_0 \text{ for CP } p & \text{if } T_{p,\min} > k_\alpha, \\ \text{ambiguous} & \text{otherwise.} \end{array} \tag{41}$$

5.2.2. *Iterative localization and stopping criterion*
In classical diagnosis, localization stops when the remaining network passes a global congruency test. In the interval framework, this criterion can be overly conservative because bounded systematic effects accumulate over the network and may lead to artificial rejection of stable points.

Therefore, the extended framework uses a local stopping criterion. Control points classified as *strictly deformed* ($T_{p,\min} > k_\alpha$) are removed iteratively until no point exceeds the local threshold. Ambiguous points are retained in the reference frame, so that unresolved systematic uncertainty is not converted into false structural alarms.

5.3. Local test in the surface domain

As established in Section 4.3, the nominal surface displacement $\hat{\boldsymbol{d}}_S(u,v)$ and its stochastic cofactor matrix $\boldsymbol{Q}_{d_S d_S}(u,v)$ are obtained via linear propagation through the B-spline basis matrix $\boldsymbol{B}(u,v)$.

Under the interval framework, the induced systematic surface bias is similarly bounded by projecting the global CP bounds ($\Delta_{\boldsymbol{d}}$) through the absolute basis functions:

$$\Delta_{\boldsymbol{b}_S(u,v)} = |\boldsymbol{B}(u,v)|\,\Delta_{\boldsymbol{d}}. \tag{42}$$

Because the tensor-product B-spline basis functions are strictly non-negative and sum to one (satisfying the convex hull property), this propagation effectively maps the exact systematic bounds to the continuous surface without introducing any artificial interval overestimation.

For any admissible surface bias $\boldsymbol{b}_S \in [-\Delta_{\boldsymbol{b}_S(u,v)}, +\Delta_{\boldsymbol{b}_S(u,v)}]$, the normalized test statistic $T_S(\boldsymbol{b}_S)$ is formulated analogously to the classical surface test (Eq. 26). The extremal values $T_{S,\min}$ and $T_{S,\max}$ are then evaluated over this bounded set, and the final surface diagnosis follows the identical ternary decision rule (Eq. 41).

5.4. Empirical validation and diagnostic results

The interval-extended procedure was applied to 1000 Monte Carlo realizations at $\alpha = 0.05$. As in the classical analysis, CP and SP results are reported separately: the CP domain uses correlation-aware local diagnosis with a local stopping criterion, whereas the SP domain provides a pointwise diagnostic map of the propagated surface deformation field. In contrast to the classical test, which forced an

Table IV. Averaged extended 2×3 confusion matrix evaluated in the CP domain. The ambiguous state absorbs points whose true status is obscured by systematic uncertainty.

Ground Truth	**Total**	**Strictly Stable**	**Ambiguous**	**Strictly Deformed**
Stable	266	212.0 (79.7%)	44.5 (16.7%)	9.5 (3.6%)
Deformed	34	0.0 (0.0%)	0.1 (0.3%)	33.9 (99.7%)

overconfident binary choice, the extended test utilizes the *ambiguous* classification as a mathematical buffer. As seen in the physically stable CP subset (Table IV), the ambiguous state (16.7%) draws from both former true negatives and former false positives. The strict false-alarm rate drops from 5.9% in the classical model to just 3.6% (9.5 points), safely below the nominal 5% expectation. Most importantly, the strictly stable misclassification on the deformed subset drops to exactly 0.0%, eradicating critical non-detections.

The spatial distribution of these decisions across the CP domain is visualized in Figure 4. The top row demonstrates how systematic noise in the stable section is largely intercepted by the ambiguous

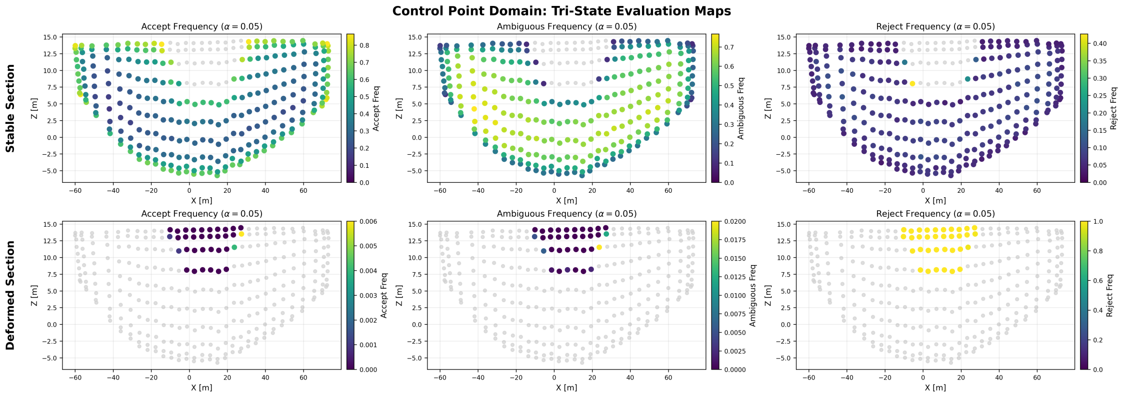

Figure 4. Spatial distribution of the extended ternary decisions in the control point domain ($\alpha = 0.05$). Top row: Evaluation frequencies on the physically stable section. Bottom row: Evaluation frequencies on the physically deformed section.

buffer. Conversely, the bottom row confirms that true deformations are never incorrectly accepted as stable.

5.4.1. *Diagnostic performance in the dense surface domain*

The protective effect of the interval framework serves its most critical role in the dense surface domain. As established in Section 4.4, because exact stochastic correlation handling is mathematically singular on the continuous surface, the required pointwise simplification leaves the diagnosis vulnerable to systematic biases.

Table V. Averaged extended 2×3 confusion matrix evaluated in the dense SP domain.

Ground Truth	Total	Strictly Stable	Ambiguous	Strictly Deformed
Stable	3609	2531.8 (70.2%)	822.6 (22.8%)	254.7 (7.1%)
Deformed	891	231.0 (25.9%)	101.2 (11.4%)	558.8 (62.7%)

The interval-extended surface test (Table V) mitigates this vulnerability by introducing the explicit ambiguous class. On the physically deformed surface, 62.7% of the points are strictly classified as deformed, while 11.4% are transferred to the ambiguous class. It must be noted that 25.9% of the true deformations are still missed (classified as strictly stable). As established in Section 4.4, this is an unavoidable physical consequence of the deformation tapering off at the boundaries of the B-spline support, where the theoretical non-centrality parameter λ drops below the Minimum Detectable Deformation threshold.

Both the classical and the interval-extended tests inherently face this exact same physical detection limit at the deformation edges. However, their behavior diverges crucially on the physically stable surface. While the classical test suffered from a cascade of false alarms (14.2%) due to unmodeled biases, the interval framework acts as a protective buffer. By assigning 22.8% of the stable points to the ambiguous class, the strict false-alarm rate is halved to 7.1%. This demonstrates the primary advantage of the extended framework: even though it cannot bypass the physical limits of detecting microscopic tapering deformations, it successfully suppresses the false positive cascade that plagues classical testing under systematic uncertainty.

The power of this ternary classification becomes particularly evident when considering sub-MDD deformations, such as a 5 mm displacement. In such a scenario, the classical test would yield a highly

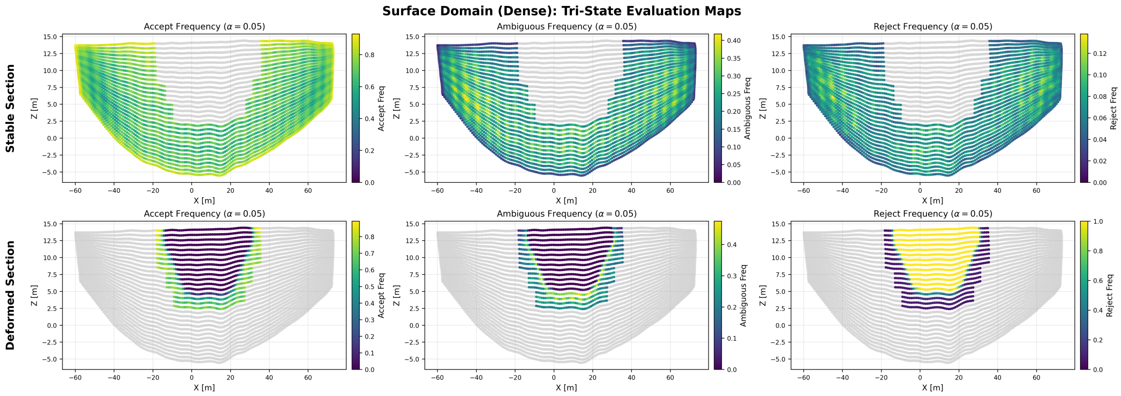

Figure 5. Spatial distribution of the extended ternary decisions in the dense surface domain ($\alpha = 0.05$). The ambiguous state absorbs regions where the decision is dominated by bounded systematic uncertainty.

unreliable mix of stochastic missed detections and systematic false alarms. The interval-extended framework, however, would correctly classify these sub-threshold movements as ambiguous. This safely informs the monitoring engineer that while a deviation exists, it cannot be rigorously separated from the system's calibration uncertainty, thereby preventing unwarranted structural alarms while maintaining continuous observation.

6. Discussion

The interval-extended congruency test changes not only the numerical outcome of the analysis, but also the interpretation of the final decision. In practical monitoring, a binary statement is often required, although the proposed framework yields a ternary outcome. In fuzzy-interval approaches, this transition is handled through a continuous rejectability measure (Neumann and Kutterer, 2009; Kutterer and Neumann, 2008). The present method uses simple interval bounds instead, so the ambiguous class defines a bounded decision space: a conservative interpretation merges ambiguity with the stable class to minimise false alarms, whereas a safety-first interpretation merges it with the deformed class to minimise missed detections. To formalise this transition, let $\alpha_{\text{strict}} = P(\text{strictly deformed} \mid H_0)$, $\beta_{\text{strict}} = P(\text{strictly stable} \mid H_1)$, $\gamma_0 = P(\text{ambiguous} \mid H_0)$, and $\gamma_1 = P(\text{ambiguous} \mid H_1)$. The empirical error rates after binary collapse are then

$$\begin{aligned} \text{Conservative:} \quad & \alpha_{\text{cons}} = \alpha_{\text{strict}}, & \qquad \text{Safety-first:} \quad & \alpha_{\text{safe}} = \alpha_{\text{strict}} + \gamma_0, \\ & \beta_{\text{cons}} = \beta_{\text{strict}} + \gamma_1, & & \beta_{\text{safe}} = \beta_{\text{strict}}. \end{aligned} \tag{43}$$

Figure 6 summarises the main effect of this transition. In the CP domain, the conservative interpretation reduces the Type I error from 5.9% to 3.6% and the Type II error from 0.6% to 0.3%; the safety-first interpretation eliminates missed detections entirely (Type II = 0.0%) at the cost of a higher false-alarm rate (Type I = 20.3%). In the SP domain the trade-off is more pronounced: the conservative interpretation reduces the Type I error from 14.2% to 7.1% while the Type II error rises to 37.3%, whereas the safety-first interpretation reduces the Type II error to 25.9% while the Type I error rises to 29.9%.

The interval-extended framework therefore does not define a single unique binary improvement over the classical test. Rather, it makes the underlying risk trade-off explicit and converts part of the classical binary misclassification into explicit uncertainty. The ambiguous class marks regions where the signal-to-bias ratio is insufficient for a reliable hard decision, allowing the final interpretation

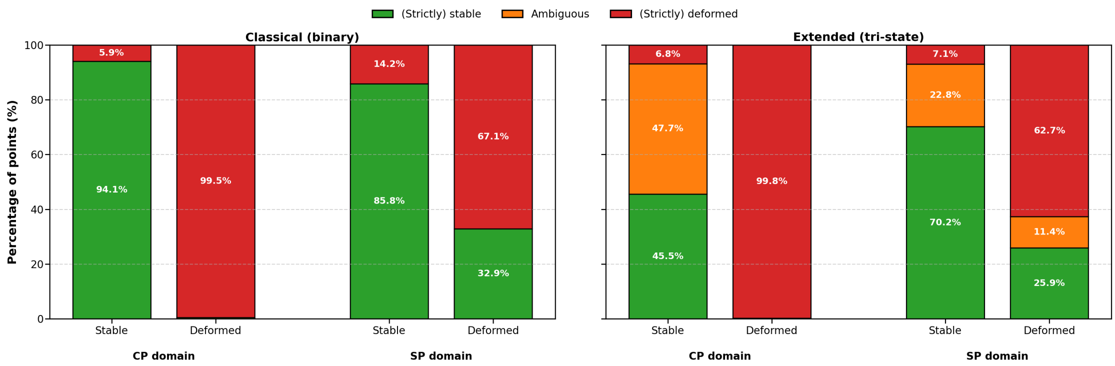

Figure 6. Comparison of the decision distribution between the classical binary approach and the interval-extended ternary approach at $\alpha = 0.05$ in the CP and SP domains.

to be aligned with the monitoring objective. From an engineering perspective, this is preferable to hiding uncertainty inside overconfident binary classifications.

7. Conclusion

Reliable TLS-based deformation monitoring requires an uncertainty model that accounts not only for stochastic measurement noise, but also for remaining systematic effects that cannot be represented confidently by a precise probability model. This study introduced an interval-extended congruency framework in which such effects are represented as unknown-but-bounded quantities and propagated from TLS influence parameters through the B-spline adjustment to the final deformation decision.

The proposed framework extends the classical binary congruency test by a ternary decision structure consisting of strict acceptance, ambiguity, and strict rejection. In the CP domain, the method is combined with a correlation-aware Schur-complement localization procedure. The results show that part of the classical binary decision can be transferred into an explicit ambiguous class, making the influence of remaining systematic uncertainty visible instead of hiding it inside a forced stable/deformed classification.

For the SP domain, the results must be interpreted more cautiously. Surface points are derived evaluations of the same CP deformation field and are not independent estimated parameters. Therefore, the SP-domain analysis was used as a pointwise diagnostic map, not as a fully correlation-aware localization procedure. The corresponding percentages should be read as descriptive indicators of the spatial expression of the deformation field, especially in the presence of remaining systematic effects and multiple pointwise tests.

Overall, the interval-extended approach does not replace the classical stochastic congruency test. Rather, it complements it by identifying cases where the available uncertainty information is insufficient for a defensible binary decision. This is particularly relevant for TLS-based monitoring scenarios in which small deformation signals, spatial dependence, and residual systematic effects occur simultaneously.

References

Baarda, W.: 1967, 'Statistical concepts in geodesy, volume 2 (4) of Publications on Geodesy'. *New Series. Netherlands Geodetic Commission, Delft, Netherlands.*

Beer, M., S. Ferson, and V. Kreinovich: 2013, 'Imprecise probabilities in engineering analyses'. *Mechanical Systems and Signal Processing* **37**(1–2), 4–29.

Caspary, W. F.: 1987, *Concepts of Network and Deformation Analysis*, No. 11 in Monograph. Kensington, N.S.W., Australia: School of Surveying, The University of New South Wales.

Harmening, C.: 2020, 'Spatio-temporal deformation analysis using enhanced B-spline models of laser scanning point clouds'. Ph.D. thesis, Technische Universität Wien.

Heunecke, O., H. Kuhlmann, W. Welsch, A. Eichhorn, and H. Neuner: 2013, *Handbuch Ingenieurgeodäsie: Auswertung geodätischer Überwachungsmessungen.* Neu bearbeitete und erweiterte auflage edition.

Kermarrec, G., B. Kargoll, and H. Alkhatib: 2020, 'Deformation analysis using B-spline surface with correlated terrestrial laser scanner observations—A bridge under load'. *Remote Sensing* **12**(5), 829.

Kutterer, H.: 1999, 'On the sensitivity of the results of least-squares adjustments concerning the stochastic model'. *Journal of Geodesy* **73**, 350–361.

Kutterer, H. and I. Neumann: 2008, 'Multidimensional Statistical Tests for Imprecise Data'. In: P. Xu, J. Liu, and A. Dermanis (eds.): *VI Hotine-Marussi Symposium on Theoretical and Computational Geodesy.* Berlin, Heidelberg, pp. 232–237, Springer Berlin Heidelberg.

Medić, T., H. Kuhlmann, and C. Holst: 2019, 'Designing and evaluating a user-oriented calibration field for the target-based self-calibration of panoramic terrestrial laser scanners'. *Remote Sensing* **12**(1), 15.

Meyer, N., T. Medic, E. Friedli, R. Senti, and A. Wieser: 2025, 'Investigation of different registration methods for TLS-based deformation analysis of hydroelectric dams – A case study'. Technical report.

Naeimaei, R. and S. Schön: 2026, 'Beyond a Pure Stochastic Treatment: Integrating Remaining Systematics into Congruency Tests'. In: *Ingenieurvermessung.*

Naeimaei, R. and S. Schön: 2025, 'Deterministic uncertainty for terrestrial laser scanning observations based on intervals'. *Journal of Applied Geodesy* **19**(3), 385–394.

Neumann, I. and H. Kutterer: 2009, 'The probability of type I and type II errors in imprecise hypothesis testing with an application to geodetic deformation analysis'. *International Journal of Reliability and Safety* **3**(1-3), 286–306.

Niemeier, W.: 2025, '50 Years of Deformation Monitoring - What has been achieved?'. Technical report.

Ötsch, E., C. Harmening, and H. Neuner: 2025, 'Employing variance component estimation for point cloud based geometric surface representation by B-splines'. *Journal of Applied Geodesy* **19**(3), 377–384.

Piegl, L. and W. Tiller: 1997, *The NURBS Book.* Berlin: Springer.

Shi, N., T. Medic, N. Meyer, A. Voordendag, and A. Wieser: 2025, 'Quantifying and Reducing the Uncertainty of 3D Displacement Estimates from Terrestrial Laser Scanner Point Clouds: A Case Study in Alpine Geomonitoring'. Technical report.